Journal of Solid State Chemistry **164,** 119–130 (2002)
doi:10.1006/jssc.2001.9455, available online at http://www.idealibrary.com on IDEAL®

The Crystal Structures, Microstructure and Ionic Conductivity of $Ba_2In_2O_5$ and $Ba(In_xZr_{1-x})O_{3-x/2}$

P. Berastegui,*[,1] S. Hull,† F. J. García-García,* and S.-G. Eriksson‡

*Department of Inorganic Chemistry, Arrhenius Laboratory, Stockholm University, S-106 91 Stockholm, Sweden; †The ISIS Facility, Rutherford Appleton Laboratory, Didcot, Oxon, OX11 0QX, U.K.; and ‡Studsvik Neutron Research Laboratory, Uppsala University, S-611 82 Nykoping, Sweden

Received April 30, 2001; in revised form October 28, 2001; accepted November 16, 2001

This paper describes the results of electron microscopy, high-temperature powder neutron diffraction, and impedance spectroscopy studies of brownmillerite-structured $Ba_2In_2O_5$ and perovskite structured $Ba(In_xZr_{1-x})O_{3-x/2}$. The ambient temperature structure of $Ba_2In_2O_5$ is found to adopt *Icmm* symmetry, with disorder of the tetrahedrally coordinated (In^{3+}) ions of the type observed previously in $Sr_2Fe_2O_5$. $Ba_2In_2O_5$ undergoes a $\sim$ 6-fold increase in its ionic conductivity over the narrow temperature range from $\sim$ 1140 K to $\sim$ 1230 K, in broad agreement with previous studies. This transition corresponds to a change from the brownmillerite structure to a cubic perovskite arrangement with disordered anions. Electron microscopy investigations show the presence of extended defects in all the crystals analyzed. $Ba(In_xZr_{1-x})O_{3-x/2}$ samples with $x = 0.1$ to 0.9 adopt the cubic perovskite structure, with the lattice parameter increasing with x. © 2002 Elsevier Science (USA)

Key Words: **$Ba_2In_2O_5$; neutron powder diffraction; electron microscopy; phase transition; ionic conductivity.**

1. INTRODUCTION

Compounds that exhibit high values of oxygen ion conductivity find widespread technological applications, including fuel cells and oxygen sensors (1). Oxides of stoichiometry ABO_3 possessing the perovskite crystal structure have attracted considerable attention, though oxygen ion disorder typically reaches significant proportions only at relatively high temperatures ($\sim$ 1000–1200 K). Attempts to enhance the mobility of the oxygen ions at more modest temperatures have focussed on the use of aliovalent cation doping to introduce charge-compensating vacancies on the oxygen sublattice. An example is the addition of Y_2O_3 to perovskite-structured $BaCeO_3$ forming $Ba(Ce_{1-x}Y_x)O_{3-x/2}$ (2).

[1]To whom correspondence should be addressed. Fax: + 46 8 152187. E-mail: pedro@inorg.su.se.

The perovskite structure is illustrated in Fig. 1a. The A and B cations are located on the 1(b) $\frac{1}{2}, \frac{1}{2}, \frac{1}{2}$ and 1(a) 0,0,0 sites of space group $Pm\bar{3}m$, respectively, with the oxygen anions in the 3(d) $\frac{1}{2}$, 0, 0 positions. As a result, the larger A cations sit at the center of a cube of 8 corner-sharing BO_6 octahedra and are surrounded by a cuboctahedron of 12 anions. The ideal cubic perovskite structure is, however, observed only if the sizes of both cation species are compatible with the sizes of their respective interstices. If r_i is the ionic radius of ion i, this requirement can be quantified using the so-called Goldschimdt tolerance factor, which should have a value close to unity (3). For t_G significantly greater than 1, the cubic perovskite structure becomes unstable and arrangements containing edge-sharing octahedra become favored, while lower values of t_G result in cooperative tilts of the octahedra to form distorted (lower symmetry) perovskite structures, such as the orthorhombic modification in space group *Pnma* adopted by $BaCeO_3$ at ambient temperature (4).

The effects of chemical doping of the B site with cations of lower valence (and the associated introduction of charge-compensating anion vacancies) on the crystal structure and ionic conducting properties of perovskite-structured oxides have been widely studied. Attempts to formulate the optimum values of, for example, t_G, the comparative radii of host and dopant cations and the vacancy concentration, to provide the highest values of ionic conductivity have been reported (5). As the dopant concentration increases there is a tendency toward ordering of the oxygen vacancies leading to a number of anion-deficient perovskite-related structures. As discussed previously (6), those of stoichiometry $A_2B_2O_5$ (i.e., $ABO_{2.5}$) form a structural family containing promising oxygen ion conductors, though they are not as widely studied as the perovskite parent compounds. There are six known vacancy patterns, in which some of the BO_6 octahedra are replaced by BO_5 square pyramids ($Ca_2Mn_2O_5$), BO_4 square planar units ($La_2Ni_2O_5$), BO_4 tetrahedra ($Ca_2Fe_2O_5$), or combinations thereof (7). The formation of

0022-4596/02 $35.00
© 2002 Elsevier Science (USA)
All rights reserved.

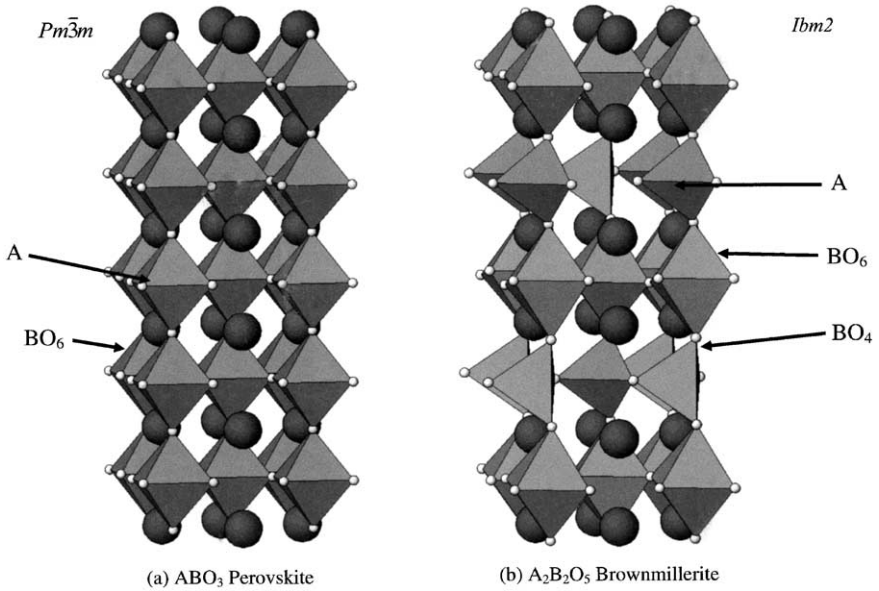

FIG. 1. Schematic diagram showing the relationship between the ABO_3 perovskite (a) and $A_2B_2O_5$ brownmillerite (b) structures. The former is converted to the latter by replacement of half the BO_6 octahedra by BO_4 tetrahedra.

BO_4 tetrahedra in the so-called brownmillerite structure is of particular relevance to the work presented in this paper and is illustrated in Fig. 1b.

In this paper we describe the results of electron microscopy, powder neutron diffraction, and impedance spectroscopy studies of brownmillerite-structured $Ba_2In_2O_5$ and the perovskite-structured solid solution $Ba(In_xZr_{1-x})O_{3-x/2}$. The brownmillerite structure is an orthorhombic superstructure of the cubic perovskite structure with $a_{\text{brownm}} \sim \sqrt{2}a_{\text{perov}}$, $b_{\text{brownm}} \sim 4a_{\text{perov}}$, and $c_{\text{brownm}} \sim \sqrt{2}a_{\text{perov}}$. As illustrated in Fig. 1b, in the b direction there is a sequence of octahedra (O) and tetrahedra (T) in the form OTOT′O … (where T and T′ are different orientations of tetrahedra). However, slight displacements of the ions away from their ideal positions are possible and the correct symmetry of brownmillerite-structured compounds has been the subject of some debate, with closely related descriptions in space groups *Ibm*2, *Icmm*, and *Pcmn* being proposed (8). These differ principally in the location of the tetrahedrally coordinated B atoms and the distortion of the surrounding four oxygen ions. The structure of $Ba_2In_2O_5$ has also been erroneously described as a cubic perovskite (9) and the addition of Zr^{4+} forms the system $Ba(In_xZr_{1-x})O_{3-x/2}$, in which the $x = \frac{2}{3}$ member (i.e., $Ba_3In_2ZrO_8$) was originally proposed to adopt a structure with a layer sequence OOTOOTO … (10). However, subsequent neutron diffraction studies indicated that the material possesses long-range cubic symmetry but that randomly oriented local domains of $\sim$ 50–500 Å in size occur due to short-range ordering of the vacancies (11).

At temperatures close to ambient both $Ba_2In_2O_5$ and $Ba(In_xZr_{1-x})O_{3-x/2}$ possess some protonic conduction (12) though at $\sim$ 600 K the ionic conductivity of $Ba(In_xZr_{1-x})O_{3-x/2}$ with $x = \frac{2}{3}$ is $\sim 10^3\times$ higher than that of $Ba_2In_2O_5$ (10). At $T \sim 1200$ K $Ba_2In_2O_5$ has been shown to undergo a first-order phase transition to a highly conductive phase ($\sigma \sim 0.1\ \Omega^{-1}\,\text{cm}^{-1}$ at $T \sim 1250$ K (13)). A detailed NMR, DTA, and X-ray diffraction study indicated the onset of oxygen ion conduction in $Ba_2In_2O_5$ at $T \sim 1198$ K, but that this involves only oxygen ions between the tetrahedral layers. The material remains orthorhombic up to $\sim$ 1348 K (though with increasing O^{2-} disorder) at which temperature it was reported to transform to the cubic perovskite structure (i.e., $BaInO_{2.5}$).

2. EXPERIMENTAL

Samples of $Ba_2In_2O_5$ and $Ba(In_xZr_{1-x})O_{3-x/2}$ with $x = 0.1$–0.9 were prepared by mixing stoichiometric amounts of $BaCO_3$, In_2O_3, and ZrO_2 and sintering in air at 1575 K for 3 days with intermediate grindings. Sample purity was confirmed using X-ray diffraction. Guinier films were taken using Cu $K\alpha_1$ radiation and analyzed with an automated scanning system. No sign of impurities could be detected except for a small amount of an impurity phase that could not be identified in the sample with highest In content ($x = 0.9$) in the series $Ba(In_xZr_{1-x})O_{3-x/2}$. These samples were also found to be slightly hygroscopic.

Two terminal measurements of the ionic conductivity of $Ba_2In_2O_5$ were performed using a pelleted sample 6 mm in

diameter and 5 mm in length. This was held between two spring-loaded platinum disks inside a boron nitride cell, which is inserted into the hot zone of a horizontal tube furnace. Details of this device can be obtained elsewhere (14). A Solartron S1260 frequency response analyzer determined the conventional Z–Z' Bode plot over the frequency range from 10^{-1} Hz to 10^{7} Hz. The real component of the sample impedance Z_S was determined using software developed in-house (14). All measurements were performed under dynamic vacuum of $\sim 10^{-4}$ bar and temperature monitoring was obtained using chromel/alumel thermocouples located ~ 2 mm from the sample pellet.

The diffraction experiments were performed on the Polaris powder diffractometer at the ISIS facility, U.K. (15), with the samples encapsulated inside thin-walled vanadium cans 11 mm in diameter and 40 mm in height. High-temperature measurements used a special furnace designed for neutron diffraction and constructed using a vanadium foil resistive heating element and heat shields. Diffraction data were predominantly collected using the backscattering detector bank which covers the scattering angles $135^\circ < \pm 2\theta < 160^\circ$ and provides data over the d-spacing range $0.5 < d$ (Å) < 3.2 with an essentially constant resolution $\Delta d/d \sim 5 \times 10^{-3}$. Rietveld profile refinements using the normalized diffraction data were performed using the program TF12LS (16), which is based on the Cambridge Crystallographic Subroutine Library (17). The quality of the fits was assessed using the usual goodness-of-fit R-factors, R_w and R_{exp} (18).

The samples used in the electron microscopy studies were prepared by grinding the samples under butanol and placing one drop of the suspension onto a holey carbon film supported by a copper grid. These grids were then examined in JEOL-3010 UHR and JEOL 2000FX transmission electron microscopes. The latter is equipped with a LINK AN10000 energy-dispersive X-ray microanalysis (EDX) system.

3. RESULTS AND DISCUSSION

3.1. *Ambient temperature structure of $Ba_2In_2O_5$*

The refinements of the powder neutron diffraction data collected at ambient temperature were initially performed using the most recently published structural model in space group *Ibm*2 (19). This places the Ba^{2+} in 8(*c*) *x*,*y*,*z* sites with $x_{Ba} \sim 0.51$, $y_{Ba} \sim 0.61$, and $z_{Ba} \sim 0.01$ and the In^{3+} are distributed equally between the octahedrally coordinated In1 in 4(*a*) 0,0,0 sites and the tetrahedrally coordinated In2 in 4(*b*) *x*, $\frac{1}{4}$,*z* sites with $x_{In2} \sim 0.56$ and $z_{In2} \sim 0.46$. The O^{2-} are located in three distinct positions: O1 in 8(*c*) sites with $x_{O1} \sim 0.26$, $y_{O1} \sim 0.99$, and $z_{O1} \sim 0.26$ which form the middle band of the octahedra; O2 in 8(*c*) sites with $x_{O2} \sim 0.06$, $y_{O2} \sim 0.14$, and $z_{O2} \sim 0.03$ which link the octahedra and tetrahedra; and O3 in 4(*b*) sites with $x_{O3} \sim 0.65$ and $z_{O3} \sim 0.11$ to form the remaining two vertices of the tetrahedra. The octahedra and tetrahedra are thus $In1(O1_4O2_2)$ and $In2(O2_2O3_2)$ units, respectively. The final fits included the 10 coefficients of a polynomial describing the background scattering, the 3 unit cell parameters *a*, *b*, and *c*, the 13 atomic position parameters which are allowed to vary by symmetry (listed above), isotropic thermal vibration parameters for all atoms, and 2 peak width parameters describing the Gaussian and Lorentzian contributions to the observed peak shape. The final R_w-factor was $\sim 2.98\%$, which does not compare favorably with the expected value $R_{exp} = 1.69\%$. In addition, the refinement was relatively unstable, with large oscillations in the positions of several of the atoms and significantly larger than expected values of the isotropic temperature factors ($B > 1$ Å^2) for the In2 and O3 sites. Attempts to vary the temperature factors anisotropically failed to converge.

As discussed previously (8), there are alternative descriptions of the brownmillerite structure in space groups *Pcmn* and *Icmm*, which have been proposed for $Ca_2Fe_2O_5$ (20) and $Sr_2Fe_2O_5$ (8), respectively. The former differs from the *Ibm*2 description in the relative displacements of the In2 and O3 atoms away from their "ideal" positions. The lowering of symmetry from body-centered to primitive means that *hkl* reflections with $h + k + l = 2n + 1$ are allowed. There is no evidence for such peaks in the diffraction data for $Ba_2In_2O_5$. However, we attempted to fit the data using this model, because these peaks are expected to be weak if the distortions are small. In *Pcmn* symmetry the Ba, O1, and O2 atoms are in 8(*d*) *x*, *y*, *z* sites, the In1 are in 4(*a*) 0,0,0 sites, and the In2 and O3 atoms are in 4(*c*) *x*,$\frac{1}{4}$,*z* sites, with positional parameters close to those listed above for the *Ibm*2 case. Refinements led to a relatively poor R_w value ($\sim 3.03\%$) and, again, rather unstable convergence and anomalously high values of the isotropic temperature factors B_{In2} and B_{O2}. Moreover, the electron microscopy investigations discussed in the next section confirmed that the symmetry is body centered.

The third structural model proposed uses space group *Icmm* and includes disorder of the InO_4 tetrahedra over two different orientations. This places the Ba and O2 in 8(*h*) *x*,*y*,0 sites, the O1 in 8(*g*) $\frac{1}{4}$,*y*,$\frac{1}{4}$ sites, and the In1 in 4(*a*) 0,0,0 sites. The $4 \times$ In2 and $4 \times$ O3 atoms are each distributed over a set of 8(*i*) *x*,$\frac{1}{4}$,*z* sites such that their mean occupancy is $\frac{1}{2}$. The fit to the data using this structural model was significantly better than that obtained using the *Ibm*2 and *Pcmn* models, giving a stable refinement with $R_w = 2.58\%$. Furthermore, the refinement remained stable if the thermal vibrations of the ions were allowed to vary anisotropically, though only in the case of the O2 sites were the deviations from an isotropic distribution significant. Inclusion of anisotropic thermal vibrations only for the O2 sites reduced the goodness-of-fit R_w-factor to 2.44%. The final values of the fitted parameters are listed in Table 1 and the quality of the fit is illustrated in Fig. 2.

TABLE 1
Summary of the Results of the Least-Squares Fit to the Powder Neutron Diffraction Data Collected from $Ba_2In_2O_5$ at Ambient Temperature ($T = 298(2)$ K)

Space group	*Icmm*
Lattice parameters	$a = 6.0991(1)$ Å, $b = 16.7365(3)$ Å, $c = 5.9622(1)$ Å
Ba in 8(*h*) *x*,*y*,0	$x = 0.5122(2)$, $y = 0.6093(1)$
Isotropic thermal parameter	$B_{iso} = 0.45(2)$ Å^2
In1 in 4(*a*) 0,0,0	
Isotropic thermal parameter	$B_{iso} = 0.25(2)$ Å^2
In2 in 8(*i*) *x*,$\frac{1}{4}$,*z*	$x = 0.5610(5)$, $z = 0.4649(5)$
Isotropic thermal parameter	$B_{iso} = 0.29(4)$ Å^2
O1 in 8(*g*) $\frac{1}{4}$,*y*,$\frac{1}{4}$	$y = 0.9922(1)$
Isotropic thermal parameter	$B_{iso} = 0.45(2)$ Å^2
Site occupancy	$m = \frac{1}{2}$
O2 in 8(*h*) *x*,*y*,0	$x = 0.0501(2)$, $y = 0.1371(1)$
Anisotropic thermal parameters	$B_{11} = 0.98(4)$, $B_{22} = 0.66(3)$, $B_{33} = 1.93(5)$, $B_{12} = 0.21(4)$ Å^2
Site occupancy	$m = \frac{1}{2}$
O3 in 8(*i*) *x*,$\frac{1}{4}$,*z*	$x = 0.6303(4)$, $z = 0.1259(4)$
Isotropic thermal parameter	$B_{iso} = 0.64(3)$ Å^2
Goodness-of-fit	$\chi^2 = 2.08$
Weighted *R*-factor	$R_w = 2.44\%$
Expected *R*-factor	$R_{exp} = 1.69\%$
Number of Bragg peaks	$N_p = 847$
Number of fitted parameters	$N_f = 35$

The structure of $Ba_2In_2O_5$ is illustrated in Fig. 3, which compares the model proposed previously in *Ibm*2 symmetry with that in *Icmm* symmetry determined in this work. In the latter case, the In2 and O3 sites have mean occupancies of $\frac{1}{2}$, though, as discussed previously (8), the most plausible explanation of this feature is the formation of domains possessing tetrahedra in one of the two orientations. The

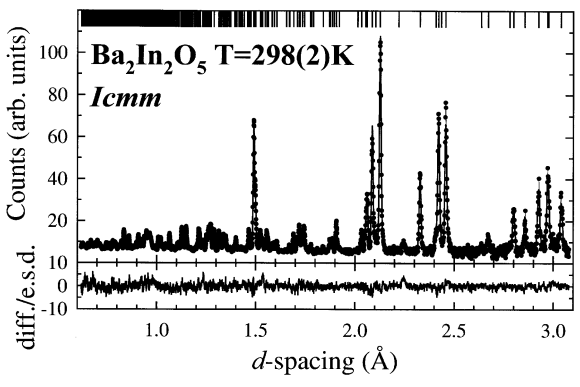

FIG. 2. Least-squares fit to the powder neutron diffraction data collected from $Ba_2In_2O_5$ at ambient temperature. The dots are the experimental data points and the solid line is the calculated profile. The lower trace shows the difference (measured minus calculated) divided by the estimated standard deviation on the experimental points and the upper tic marks denote the calculated position of the expected reflections.

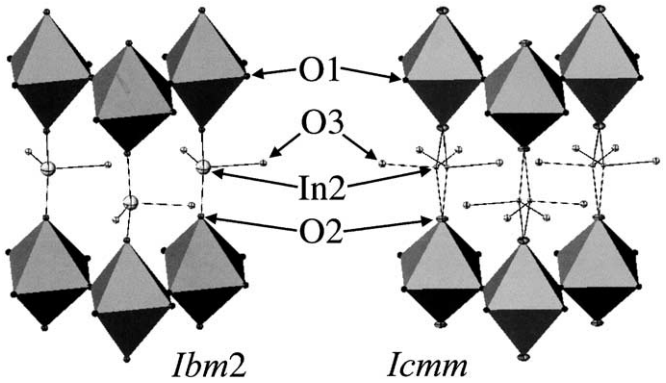

FIG. 3. Refined models of $Ba_2In_2O_5$ in *Ibm*2 and *Icmm* symmetry determined in this work. In the latter case, the In2 and O3 sites have mean occupancies of $\frac{1}{2}$.

anisotropic thermal vibrations of the O2 atoms are clearly seen in Fig. 3, with the thermal ellipsoid "flattened" perpendicular to the [010] direction. It is likely that this reflects static disorder of these ions, since they link the (disordered) InO_4 tetrahedra to the InO_6 octahedra. However, attempts to refine the diffraction data using "split" sites (with isotropic thermal vibrations) to model the anion distribution at the O2 positions were not successful, owing to excessive correlations between the positional and thermal vibration parameters of these atoms.

In this work we find that the two In^{3+}-centered polyhedra in $Ba_2In_2O_5$ are significantly more regular than proposed previously using *Ibm*2 symmetry (19). The octahedral units have In–O distances of 2.136 Å (×4) and 2.315 Å (×2) (compared with 1.882 Å (×2), 2.398 Å (×2), and 2.425 Å (×2)) and the tetrahedral ones have In–O distances of 2.018 Å (×2), 2.065 Å (×1), and 2.113 Å (×1) (compared with 1.912 Å (×2), 2.010 Å (×1), and 2.354 Å (×1)). Furthermore, the extent of the polyhedral distortions is found to be comparable to those observed in $Sr_2Fe_2O_5$, which has also been determined to adopt *Icmm* symmetry (8). A better model of the structure is thus obtained using a higher symmetry space group that allows a description of the defects inherent in the brownmillerite structure using "split" positions at the tetrahedral layers. The electron microscopy studies described below confirm the presence of distortions in the brownmillerite structure, and support the conclusion that the brownmillerite structure contains extended defects that give rise to both short- and long-range order which cannot be fully described by bulk diffraction methods.

3.2. *TEM Investigations of $Ba_2In_2O_5$*

All the crystals analyzed in the $Ba_2In_2O_5$ sample showed reciprocal lattices corresponding to the brownmillerite-type structure and extra features that changed from crystallite to

crystallite. Careful analyses of the reciprocal lattices were carried out in a large number of crystals, which allowed us to find up to three different, but closely related, types of crystals. EDX analyses showed a constant Ba/In ratio in agreement with the nominal composition of the sample.

The symmetry and extinction conditions found in the reciprocal lattice associated with the basic orthorhombic structure is in agreement with the refinements of powder neutron diffraction data. The absence of reflections $0kl$, with $k = 2n + 1$, down [100] (Fig. 4f), and $h0l$, with $h + l = 2n + 1$ (h *and* l not equal to zero), down [010] (Fig. 4a), confirms an I-centered space group, i.e., $Ibm2$ or $Icmm$.

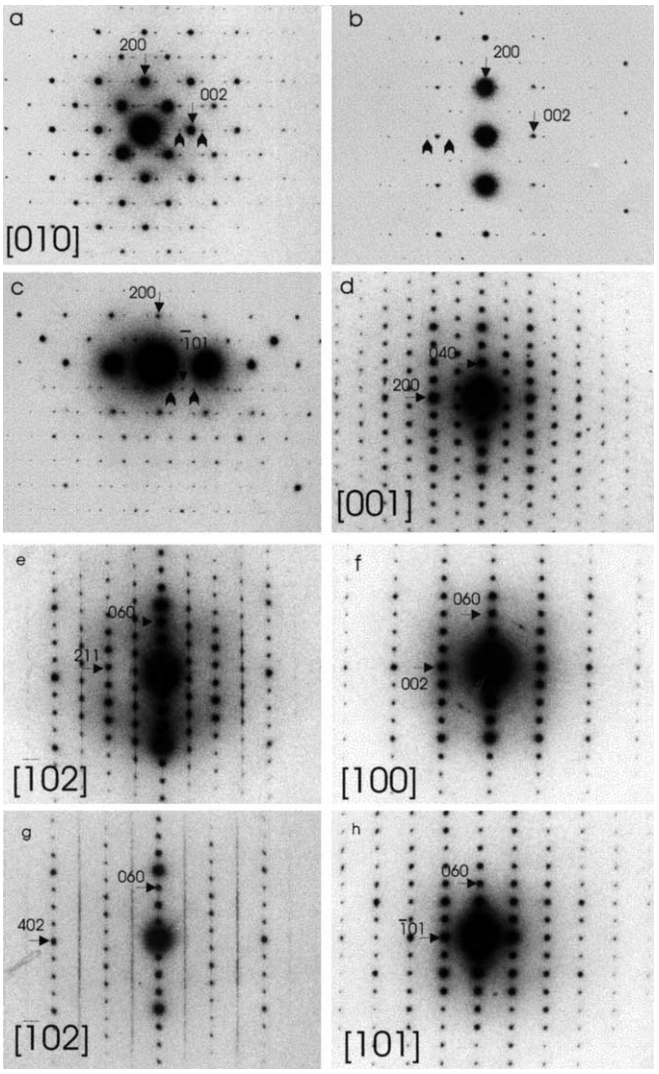

FIG. 4. (a) [010], (d) [001], (e) and (g) [$\bar{1}$02] (from different crystals), (f) [100], and (h) [101] zone axis electron diffraction patterns (EDPs) indexed according to the underlying orthorhombic brownmillerite structure. (b) and (c) correspond to the same reciprocal direction shown in (a) but slightly away from the exact Bragg condition. In (c) satellite reflections flanking $\bar{1}01$ reflections are shown by arrows. These are missing in $00l$ reflections while in (b) they are still observed.

In Fig. 4a, the [010] zone axis electron diffraction pattern (EDP) of the more abundant type of crystals is shown. Apparent satellite reflections of the form $\mathbf{G} \pm \frac{1}{4}$ [002]* are present, where **G** refers to the strong Bragg reflections of the basic orthorhombic structure. Slight tilts away from the exact [010] Bragg condition keeping **c*** excited (Fig. 4c) make satellites flanking $00l$ reflections (with l even) disappear, while the same tilt experiment keeping **a*** excited does not cause any satellites to disappear (Fig. 4b). Furthermore, tilting experiments down directions parallel to the **a***c* plane show that such satellites are not reflections but cutting points of the Ewald sphere with lines composed of reflections streaking along [010]* and sited at $\mathbf{q} \sim \pm \frac{1}{4}$ [402]* when looking down [010]. These reflections are perfectly commensurate with the basic orthorhombic cell and can be indexed with a vector $\mathbf{q} = \frac{1}{2}$ [211]*. From these experiments, satellite reflections seen along the exact [010] Bragg condition shown in Fig. 4a should be interpreted as created by double diffraction from $h0l$ (h and l not equal to zero) reflections plus a scattering vector of the form $\sim \pm \frac{1}{4}$ [40 $\pm$ 2]. Such an interpretation is in agreement with the tilting experiments shown in Figs. 4b and 4c. A close inspection of the neutron diffraction pattern shows indeed a very weak reflection at 5.35 Å that corresponds to twice the spacing of the 211 reflection. Much more disordered crystals with continuous lines of diffuse scattering at the same reciprocal positions were also observed (Figs. 4e and 4g).

In Fig. 5a, we present a [010] zone axis EDP from a crystal showing satellite reflections sited at $\mathbf{G} \pm \frac{1}{3}$ [002]*. Tilting experiments gave results similar to those discussed above. Slight movements of the incident beam probe bring up much weaker satellites of the form $\mathbf{q} = \pm \frac{1}{4}$ [002]* and differences in the satellite intensity, which suggests the presence of domains. Such domains should be present in a rather fine scale and a single crystal presenting only one extra vector $\mathbf{q} = \pm \frac{1}{3}$ [002]* was never found. In Fig. 5b we present an EDP recorded a few degrees away from the exact Bragg condition presented in Fig. 5a. The appearance of satellites of the form $\mathbf{q} = \pm \frac{1}{4}$ [002]* is indicated, while the satellites present in Fig. 5a have disappeared. This suggests that the former satellite reflections ($\mathbf{q} = \pm \frac{1}{3}$ [002]*) are lying in the **a***c* plane and the latter ($\mathbf{q} = \pm \frac{1}{4}$ [002]*) are slightly out of the plane, in accordance with a doubling along [211]*. Along perpendicular directions, the [$\bar{1}$03] zone axis is the only reciprocal direction giving clear differences that would help us to confirm that both extra vectors coexist. These are shown in Fig. 5c, where lines of sharp reflections running parallel to [010] and sited at $\mathbf{q} = \pm \frac{1}{3}$ [301]* are present as well as lines appearing toward the edge of the pattern that correspond to the cutting points sited at $\mathbf{q} = \pm \frac{1}{4}$ [002]* when looking along [010].

A different type of crystal with short lines of diffuse scattering running along [001]* was also found in the sample, see Fig. 6a. Slight tilts away from the exact [010]

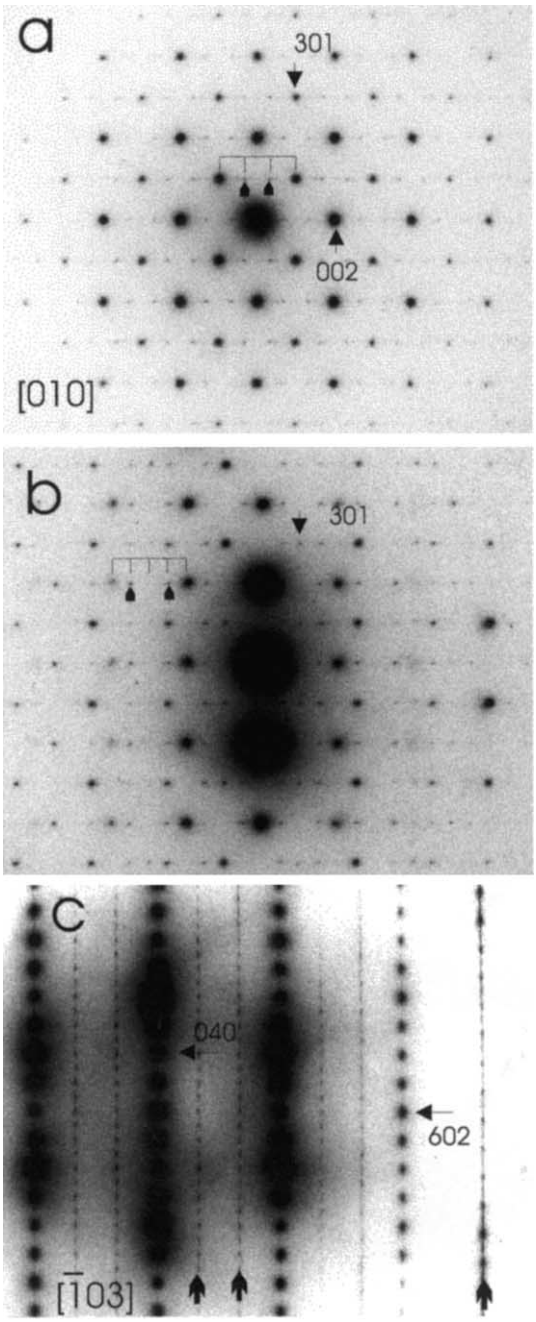

FIG. 5. (a) [010] and (c) [$\bar{1}$03] zone axis EDPs showing an extra vector of the type $\mathbf{q} = \frac{1}{3}$[002]*. (b) was taken a few degrees away from the exact Bragg condition shown in (a). The appearance of satellites of the type $\mathbf{q} = \frac{1}{4}$ [002]* is shown by arrows. In (c) the coexistence of both vectors in the same crystal is confirmed, the former lying in the plane and the latter slightly out of the plane.

zone axis orientation bring up lines running along this direction, as shown in Figs. 6b, 6c, and 6d. *h*0*l* and *h*1*l* reflections are thus connected by lines of diffuse scattering and weak satellite reflections. In Figs. 6e and 6f, two EDPs taken on the same crystal tilted around [100]* are shown and can be interpreted as two-dimensional surfaces of diffuse scattering running parallel to **c*** and cutting the **a*****b*** plane as can be seen in Fig. 6a. Moreover, in the pattern presented in Fig. 6a, at the exact Bragg condition, the diffuse intensity seems to peak at $\sim\frac{1}{3}$ [002]*, this being the endpoint, while the extra vector $\sim\frac{1}{4}$ [002]* is sited within the diffuse intensity distribution.

A direct relationship between all peculiarities observed in reciprocal space can thus be explained in terms of satellite reflections condensing out in different reciprocal positions that give rise to two different commensurate superstructures. These observations are related to those described previously in topologically related compounds (21, 22) and in a brownmillerite-type structure (23). The superstructure defined by a vector of the form $\mathbf{q} = \frac{1}{3}$ [002]* should correspond to the structure represented in Fig. 8 of Ref. (21). However, the superstructure defined by $\mathbf{q} = \frac{1}{2}$ [211]* has never been reported before. Furthermore, we do not observe

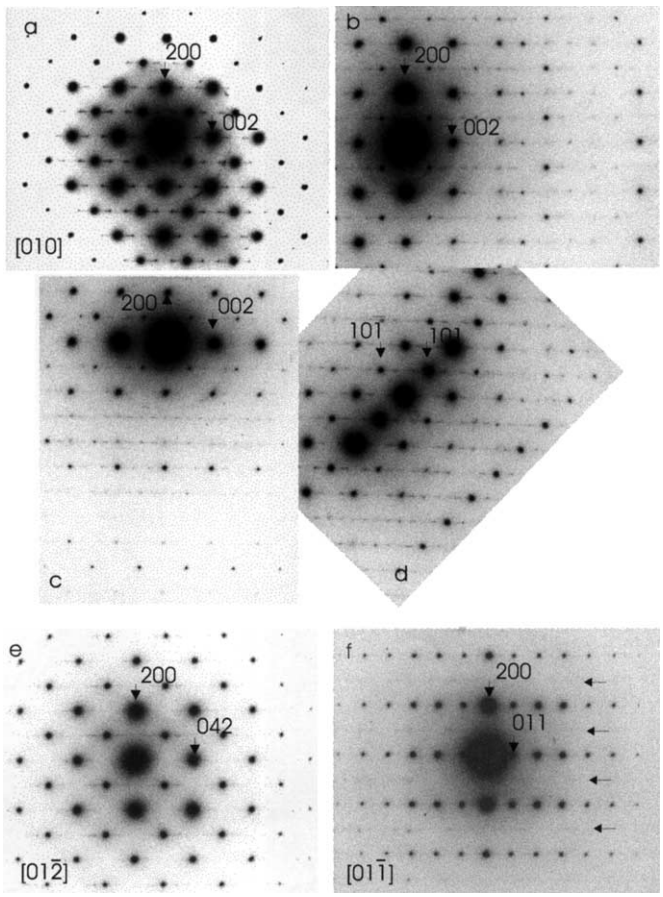

FIG. 6. (a) [010], (e) [01$\bar{2}$], and (f) [01$\bar{1}$] zone axis EDPs of the third type of crystal found in $Ba_2In_2O_5$. In this case, short lines of diffuse scattering running parallel to the [001]* reciprocal direction can be seen in (a). The endpoint of these lines is $\sim\frac{1}{3}$ [002]* and the tilting experiments combined with different projections of the reciprocal lattice show the three-dimensional shape of such diffuse scattering. Along [01$\bar{1}$] in (f) the arrows indicate lines of weak diffuse scattering.

any superstructural ordering along the main directions of the basic orthorhombic structure.

In Fig. 7a, a high-resolution image along [101] of a crystal of $Ba_2In_2O_5$ is shown together with the corresponding zone axis EDP (Fig. 7b). The presence of satellite reflections of the form $\mathbf{q} = \frac{1}{2}[211]^*$ was confirmed by tilting the crystal a few degrees away from the exact Bragg condition and keeping $\mathbf{b}^*$ excited, see Fig. 7c. The lines of reflections appearing in this experiment can be compared with the pattern presented in Fig. 4a and should correspond to satellites flanking $\bar{1}01$ and $10\bar{1}$ reflections. The imaged crystal presents an antiphase boundary, suggesting that locally the contact between octahedra and tetrahedra can occur within the planes. However, these defects were rarely found and were detectable only in the microscope when working in image mode.

In Fig. 8a, a high-resolution image of a $Ba_2In_2O_5$ crystal oriented along $[\bar{1}02]$ is shown with the corresponding FFT in the inset. Apparently, the crystal presents a well-ordered microstructure when looking at the image. However, the FFT presents lines of diffuse scattering running along the rows of reflections defining the superstructure, which are not present in the rows of reflections belonging to the basic brownmillerite-type structure. In Fig. 8c an enlarged area of the same picture is presented. The observed contrast is composed of broad white lines with dotted lines in between. This suggests that the dotted lines correspond to the tetrahedral layers and the defects in Fig. 8c could then be explained as stacking faults. A high-resolution image from

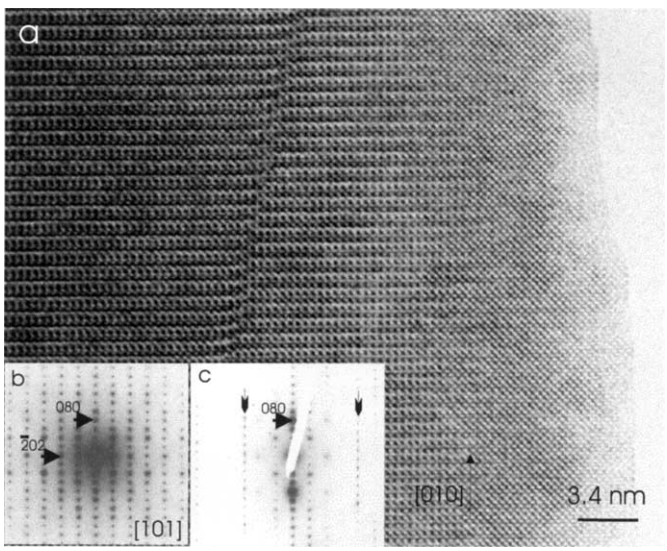

FIG. 7. (a) High-resolution image of a crystal of $Ba_2In_2O_5$ oriented along the [101] direction of the basic orthorhombic structure. The corresponding zone axis EDP is shown in (b) and in (c) after tilting the crystal a few degrees away of the exact Bragg condition and keeping $\mathbf{b}^*$ excited. Note the additional reflections between the ZOLZ (zero-order Laue zone) and FOLZ (first-order Laue zone).

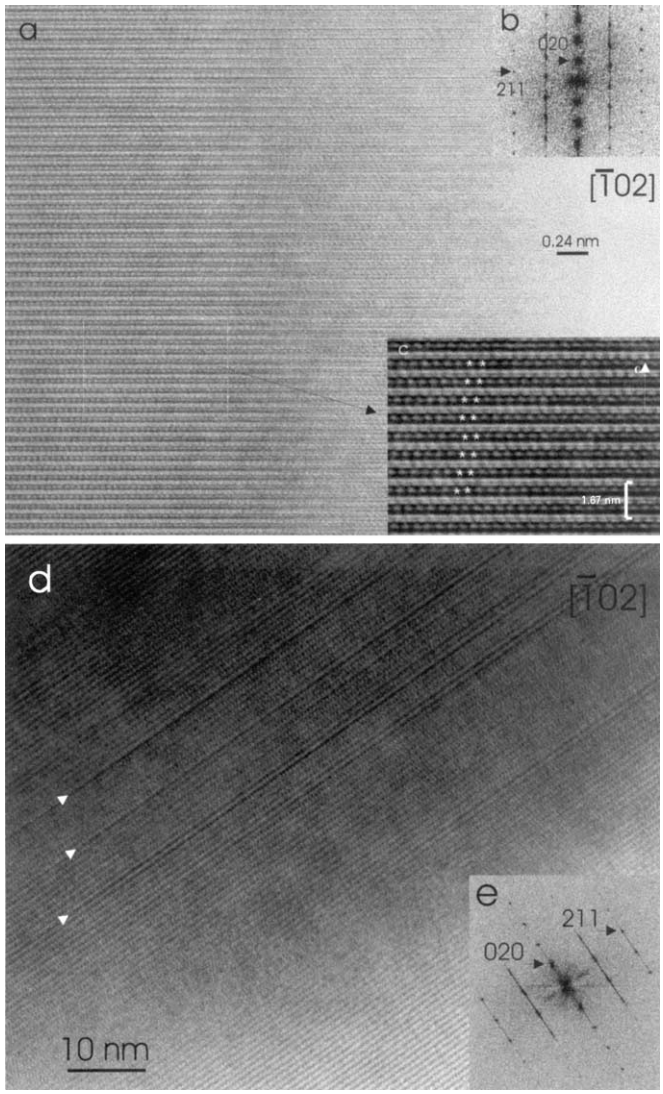

FIG. 8. (a) High-resolution image of a crystal of $Ba_2In_2O_5$ oriented along $[\bar{1}02]$. In (b) the FFT (fast Fourier transform) of the image is shown. The area marked in (a) is enlarged in (c) where the presence of stacking faults is shown. In (d) a high-resolution image of a different crystal oriented along the same direction is shown with planar defects indicated by arrows. In (e) the corresponding FFT is shown.

a different crystal oriented along the same direction is presented in Fig. 8e where plane defects can be clearly distinguished. In this case the FFT present lines of diffuse scattering running along rows of basic and satellite reflections due to the presence of extended plane defects.

Twin domains are often found in perovskite-related materials, even when the structure presents an orthorhombic distortion of the basic cubic perovskite structure as in the case of $Ba_2In_2O_5$, and many examples are described in the literature, see e.g. Ref. (21). A high-resolution image taken on a crystallite of $Ba_2In_2O_5$ showing twin domains is presented in Fig. 9. The homogeneous contrast across the twin

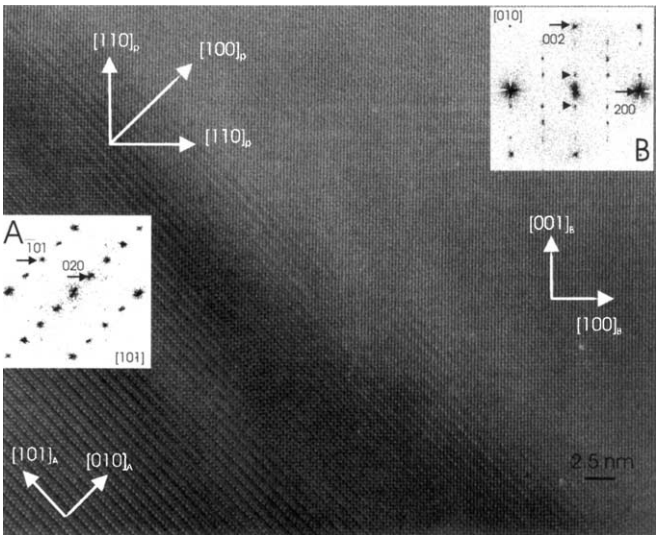

FIG. 9. High-resolution image of a crystal of $Ba_2In_2O_5$. In the insets, digital diffractograms corresponding to each area are presented. In B, satellites are indicated with arrows. Directions in a cubic perovskite are also shown (subindex p). Note that the $[\bar{1}01]$ direction is in common and the [010] in A corresponds to [101] in B. Subindexes A and B represent the directions in the respective twin domains.

boundary suggests that the twin boundary does not involve any associated stress. The digital diffractograms belonging to each domain are shown in the insets. Note how in the inset B, the satellite reflections mentioned before are present while in inset A, only strong Bragg reflections from the underlying orthorhombic structure appear. From these digital diffractograms, crystallographic relationships can be worked out in terms of a basic cubic perovskite structure (24). Thus, a twin boundary relating the [101] with the [010] direction can be formed only by breaking the OTOT′… stacking sequence and tilting a domain 90° with respect to the other domain. Many crystals presented a different type of twin, with the [101] and [100] directions being related by the twin and the [010] direction as the common direction between the twin domains. The possibility of such twin domains was also described in Ref. (22).

Neutron powder diffraction data refinements in the *Icmm* space group result in a structural model based on a brownmillerite-type structure, but with split positions within the tetrahedral layers and halved occupancies for the ions at these positions, that can be interpreted as disordered tetrahedral layers. Tetrahedral chains with reverse polarity have been reported for related compounds (21). Furthermore, extended defects that give rise to sheets of diffuse scattering have also been reported before in a compound with the brownmillerite-type structure (23). In analogy with these results, we should point out that in the present case these extended defects are responsible for all the extra features observed in the reciprocal lattice as well as the adoption of the *Icmm* symmetry in the neutron powder data refinements. However, the lack of superstructural ordering along the major directions of the underlying orthorhombic brownmillerite-type structure prevents us from proposing a possible model in real space.

3.3. *High-temperature behavior of $Ba_2In_2O_5$*

Typical data for the ionic conductivity σ of $Ba_2In_2O_5$ over the temperature range $\sim 600 < T(\mathrm{K}) < 1300$ are illustrated in Fig. 10. At lower temperatures the σ values are rather irreproducible on repeated heating/cooling cycles, due to the presence of protonic conduction associated with moisture incorporated into the sample during prior exposure to the atmosphere (12). The data presented in Fig. 10 are in fair agreement with those published previously, though the sharp transition observed at 1203 K by Goodenough *et al.* (10) is here found to be more gradual, occurring over a temperature range from ~ 1140 K to ~ 1230 K. In addition, we observe a somewhat smaller increase in σ at the transition ($\sim 6\times$ compared to over an order of magnitude (10)).

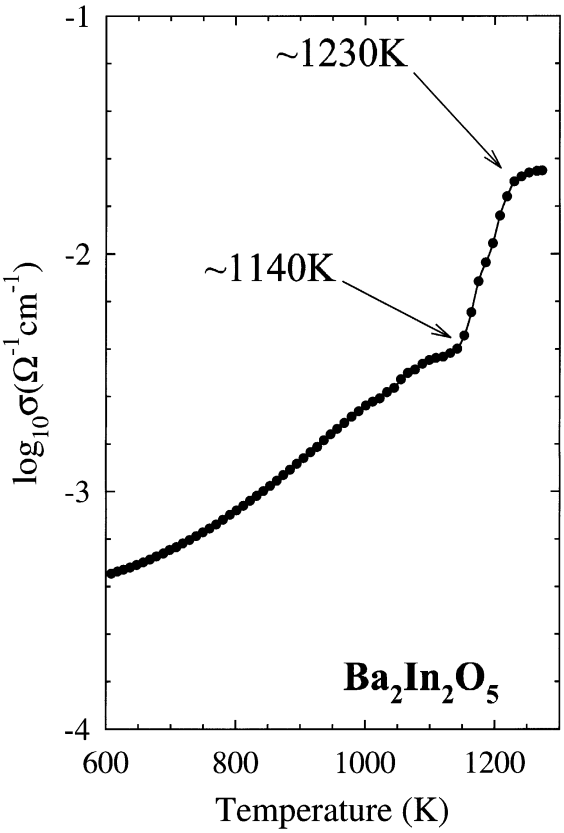

FIG. 10. Variation of the ionic conductivity σ of $Ba_2In_2O_5$ with temperature showing the abrupt increase between ~ 1140 K and ~ 1230 K.

The thermal expansion of the brownmillerite-structured $Ba_2In_2O_5$ is illustrated in Fig. 11, using the pseudo-perovskite reduced lattice parameters $a_{Br}/\sqrt{2}$, $b_{Br}/4$, and $c_{Br}/\sqrt{2}$. These appear to increase almost linearly and isotropically, with no anomalous behavior of the type observed in $Sr_2Fe_2O_5$, and are attributed to the gradual formation of tetragonally distorted perovskite phase (25). As illustrated in Fig. 12, on increasing temperature the powder neutron diffraction patterns become much simpler above ~ 1170 K, indicating a structural transformation in this temperature region. Least-squares refinements of the data collected above the transition at $T = 1250(7)$ K (see Fig. 13) confirmed that $Ba_2In_2O_5$ adopts a disordered cubic perovskite arrangement, with anisotropic thermal vibrations of the O^{2-} (see Fig. 14). Results of the Rietveld analysis are presented in Table 2. The temperature variation of the lattice parameters (Fig. 11) indicates that the transition is of first order, though there is some coexistence of the two phases over a temperature range of ~ 100 K. Unfortunately, insufficient data were collected over the transition temperature range to refine the fractions of each phase present. It should be noted that at high temperatures, the material seems to degrade after relatively short periods of time and an unknown impurity phase forms.

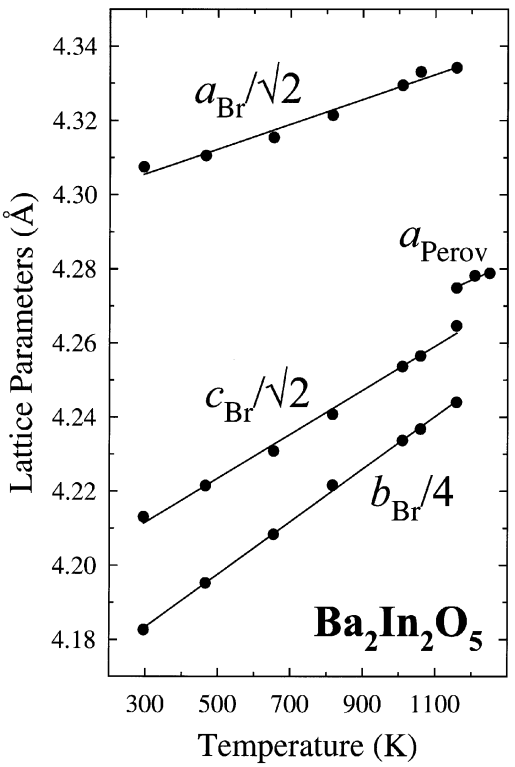

FIG. 11. Variation of the lattice parameters of the brownmillerite and perovskite phases of $Ba_2In_2O_5$ with temperature. The three values for the orthorhombic brownmillerite-structured phase (a_{Br}, b_{Br}, and c_{Br}) are referred to the perovskite substructure as shown. The discontinuous nature of the brownmillerite↔perovskite transition is apparent.

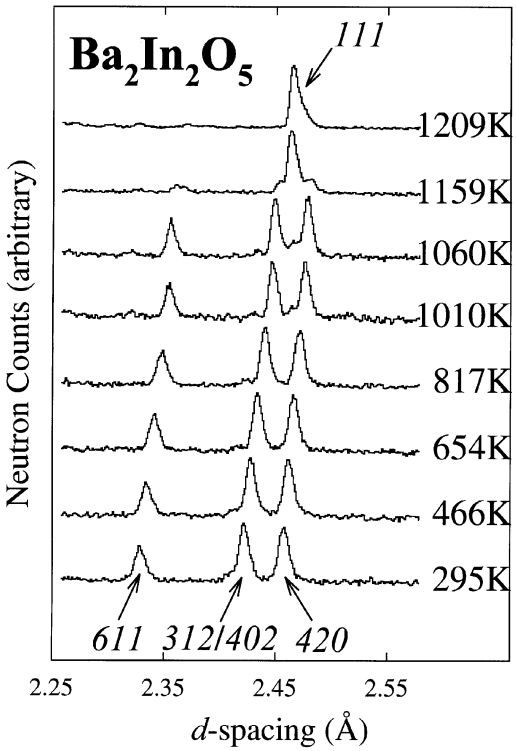

FIG. 12. Evolution of part of the powder neutron diffraction pattern of $Ba_2In_2O_5$ with temperature, illustrating the structural change from brownmillerite to disordered perovskite at ~ 1170 K. The *hkl* indices of the reflections from the brownmillerite and perovskite phases are shown at the bottom and top of the figure, respectively.

The previous high-temperature X-ray diffraction and NMR study of $Ba_2In_2O_5$ by Adler *et al.* (13) proposed a slightly different model for the transition to the highly conducting state. Their X-ray diffraction data showed that the material does not become cubic until a higher temperature of ~ 1350 K is reached. On this basis, their NMR data were interpreted in terms of the onset of two-dimensional oxygen ion disorder within the O3 layers at ~ 1200 K. This disorder starts abruptly and gives rise to the steep increase in σ at that temperature. On increasing temperature the O1 and O2 sites gradually become mobile and contribute to the conduction process until complete O^{2-} disorder occurs at ~ 1350 K and the material becomes cubic.

In this work we clearly observe the pure (disordered) cubic perovskite-structured phase at a much lower temperature and the gradual rise in σ over the temperature range from ~ 1140 K to ~ 1230 K is due to a gradual increase in the proportion of the cubic phase at the expense of the orthorhombic one. The possibility of oxygen ion disorder within the O3 layers as proposed by Adler *et al.* (13) could, on the basis of the structural model presented in the previous section, be attributed to dynamic reorientation of the

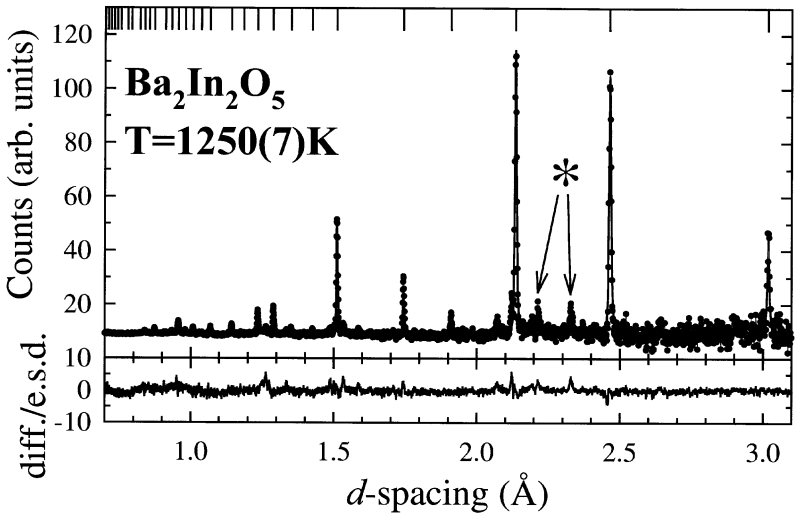

FIG. 13. Least-squares fit to the powder neutron diffraction data collected from $Ba_2In_2O_5$ at 1250(7) K using the disordered perovskite structural model. The dots are the experimental data points and the solid line is the calculated profile. The lower trace shows the difference (measured minus calculated) divided by the estimated standard deviation on the experimental points and the upper tic marks denote the calculated position of the expected reflections. The weak extra reflections denoted by * are due to an unidentified impurity that forms when the sample is kept at high temperature.

InO_4 tetrahedra over the two possible arrangements illustrated in Fig. 3. Clearly, more detailed diffraction measurements over this temperature region are required to clarify this situation, preferably with simultaneous measurements of the ionic conductivity σ to eliminate possible thermometry differences between the measurements. However, analysis of the Bragg diffraction intensities (which determine the time-averaged structure of the material under investigation) cannot directly differentiate between dynamic disorder of the tetrahedra (reorientation) or static disorder due to the presence of domains.

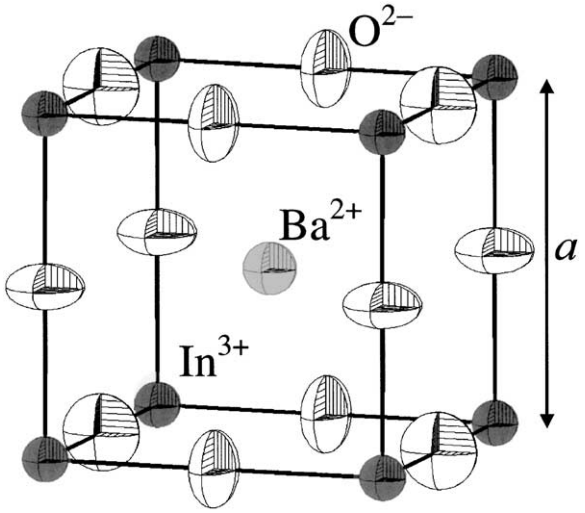

FIG. 14. Structure of the high-temperature disordered perovskite phase of $Ba_2In_2O_5$ illustrating the anisotropic thermal vibrations of the O^{2-} sites, which have an average occupancy of $\frac{5}{6}$.

3.4. Effects of Zr Doping in the Structure of $Ba_2In_2O_5$

The X-ray patterns for the samples in the $Ba(In_xZr_{1-x})O_{3-x/2}$ series could be indexed with a cubic unit cell and showed that the unit cell volume increased with increasing In^{3+} content as expected from the difference in ionic radii ($r_{In^{3+}} = 0.80$ Å, $r_{Zr^{4+}} = 0.72$ Å) (26). Figure 15 shows the change in unit cell volume as a function of In^{3+} content where the unit cell volume for $Ba_2In_2O_5$ is included as V/Z. A behavior similar to the one reported by Manthiram *et al.* (12) is observed. Thus, with increasing In^{3+} content the unit cell volume increases linearly up to about $x = 0.5$, at which point a rapid increase is observed,

TABLE 2
Summary of the Results of the Least-Squares Fit to the Powder Neutron Diffraction Data Collected from $Ba_2In_2O_5$ at 1250(7) K Using the Disordered Perovskite Structure Model

Space group	$Pm\bar{3}m$
Lattice parameter	$a = 4.27881(9)$ Å
Ba^{2+} in 1(*b*) $\frac{1}{2}, \frac{1}{2}, \frac{1}{2}$	
Isotropic thermal parameter	$B_{iso} = 3.45(9)$ Å^2
In^{3+} in 1(*a*) 0,0,0	
Isotropic thermal parameter	$B_{iso} = 2.56(8)$ Å^2
O^{2-} in 3(*d*) $\frac{1}{2}$,0,0	
Anisotropic thermal parameters	$B_{11} = 2.5(1)$, $B_{22} = B_{33} = 7.5(1)$ Å^2
Site occupancy	$m = \frac{5}{6}$
Goodness-of-fit	$\chi^2 = 1.13$
Weighted *R*-factor	$R_w = 2.89\%$
Expected *R*-factor	$R_{exp} = 2.72\%$
Number of Bragg peaks	$N_p = 56$
Number of fitted parameters	$N_f = 13$

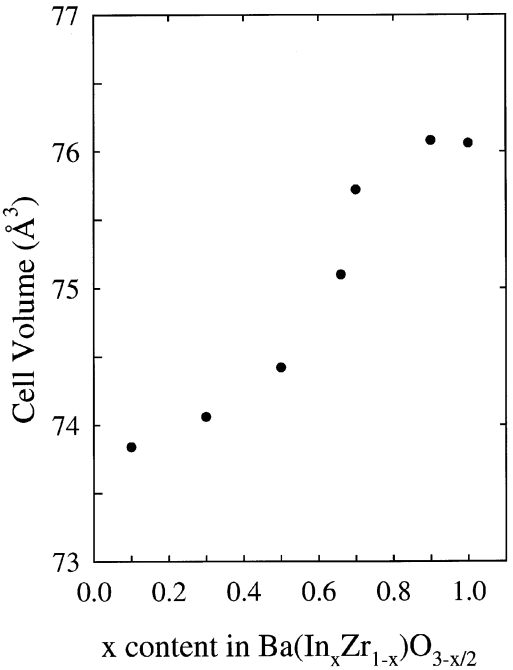

FIG. 15. Variation of the unit cell volume of $Ba(In_xZr_{1-x})O_{3-x/2}$ samples versus x.

most likely due to the increased hygroscopic nature of the material and the corresponding absorption of water into the structure.

The sample with composition $Ba(In_{2/3}Zr_{1/3})O_{8/3}$ was also studied using neutron diffraction. At ambient temperature, a structural distortion due to the absorption of moisture was observed and data were collected at 775(5) K where the distortion was no longer observed. The refinements of the data followed the same strategy adopted for the analysis of the high-temperature data for $Ba_2In_2O_5$ (section 3.3) with the $In^{3+} + Zr^{4+}$ randomly distributed over the B sites of the perovskite structure. Attempts to vary the In^{3+}/Zr^{4+} occupancies (with the anion content varied but constrained to give overall charge neutrality) did not produce a significant reduction in the goodness-of-fit R_w-factor and were abandoned. The results of the Rietveld analysis are presented in Table 3 and the quality of the fit is illustrated in Fig. 16. No displacement of the oxygen ions was observed at this temperature (11) although anisotropic thermal vibrations of the O^{2-} ions are observed. The latter appear to be even more extreme than those observed in the high-temperature $BaInO_{2.5}$ phase. Presumably, the thermal vibrations are, to some extent, modelling "static" disorder caused by slightly differing equilibrium positions of the anions dependent on the identity of their particular surrounding cations (In^{3+} and/or Zr^{4+}). Clearly, studies of a range of samples of differing In^{3+}/Zr^{4+} contents would provide information on the gradual onset of local ordering

TABLE 3

Summary of the Results of the Least-Squares Fit to the Powder Neutron Diffraction Data Collected from $Ba(In_{2/3}Zr_{1/3})O_{8/3}$ at 775(5) K

Space group	$Pm\bar{3}m$
Lattice parameter	$a = 4.23452(6)$ Å
Ba^{2+} in 1(b) $\frac{1}{2}, \frac{1}{2}, \frac{1}{2}$	
Isotropic thermal parameter	$B_{iso} = 1.92(4)$ Å^2
In^{3+}/Zr^{4+} in 1(a) 0,0,0	
Isotropic thermal parameter	$B_{iso} = 0.88(8)$ Å^2
O^{2-} in 3(d) $\frac{1}{2}$,0,0	
Anisotropic thermal parameters	$B_{11} = 0.45(3)$, $B_{22} = B_{33} = 3.85(1)$ Å^2
Site occupancy	$m = \frac{8}{9}$
Goodness-of-fit	$\chi^2 = 1.67$
Weighted R-factor	$R_w = 1.24\%$
Expected R-factor	$R_{exp} = 0.96\%$
Number of Bragg peaks	$N_p = 130$
Number of fitted parameters	$N_f = 20$

of the anion vacancies and such measurements are planned for the future.

4. CONCLUSIONS

The structural change from the brownmillerite to the perovskite structure in $Ba_2In_2O_5$ is associated with an abrupt increase in conductivity, which can be attributed to the corresponding increase in the number of anions that become mobile in the cubic phase. The transition is of first-order although both phases coexist within the range 1050 to 1175 K. No evidence of an intermediate tetragonal phase was observed from our powder neutron diffraction data. The material itself is hygroscopic and a proton conductor at low temperatures. Repeated heating cycles up to

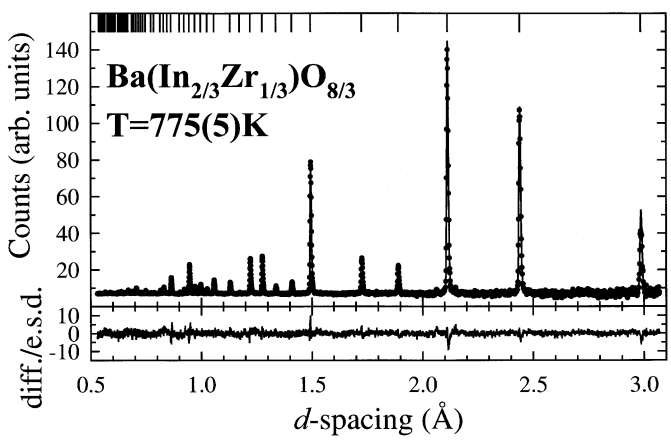

FIG. 16. Least-squares fit to the powder neutron diffraction data collected from $Ba(In_{2/3}Zr_{1/3})O_{8/3}$ at 775(5) K. The dots are the experimental data points and the solid line is the calculated profile. The lower trace shows the difference (measured minus calculated) divided by the estimated standard deviation on the experimental points and the upper tic marks denote the calculated position of the expected reflections.

775 K in an inert atmosphere were thus necessary in order to remove the absorbed species and obtain reliable anion conductivity data.

Refinements of the brownmillerite structure at ambient temperature in space group *Icmm* gave a significantly better model than when using the *Ibm*2 and *Pcmn* models, with more regular polyhedra around In^{3+} and distortions comparable to those observed in $Sr_2Fe_2O_5$. Above the transition temperature, $Ba_2In_2O_5$ adopts a disordered cubic perovskite arrangement with anisotropic thermal vibrations of the O^{2-} ions.

A rather complicated microstructure has been found by electron microscopy, and two different commensurate superstructures and a short-range order superstructure have been identified. The interpretation of the features appearing in reciprocal space can be done in analogy with similar cases described in the literature (21–23) and based on the existence of tetrahedral chains with reverse polarity. Such a disordered model is consistent with the structural refinements carried out using neutron powder diffraction data. However, a model of the superstructure defined by $\mathbf{q} = \frac{1}{2}[211]^*$ in real space that would explain all the diffracted intensity observed in the electron diffraction experiments is complex and new building principles should be worked out on one hand due to the absence of superstructural ordering along the principal directions of the brownmillerite-type structure (except along [010]) and on the other hand due to the rather unusual superstructure direction.

Furthermore, introducing a higher valence ion, such as Zr^{4+}, into the structure induces anionic disorder that transforms the structure to a defect perovskite structure as the high-temperature phase of $Ba_2In_2O_5$. In the case of Zr, the volume decreases with increasing Zr content and the oxygens introduced into the structure to maintain the charge balance are responsible for the initial increase in conductivity and lowering of the activation energy (12). At higher Zr contents, the conductivity rapidly decreases as the number of diffusion pathways is reduced and the number of mobile species increases (12).

ACKNOWLEDGMENTS

We are grateful to J. Dreyer for assistance with the high-temperature neutron diffraction measurements. One of the authors (P.B.) wishes to thank the Swedish Research Council for financial support.

REFERENCES

1. S. Chandra, "Superionics Solids: Principles and Applications." North-Holland, Amsterdam, 1981.
2. K. S. Knight, M. Soar, and N. Bonanos, *J. Mater. Chem.* **2,** 709 (1992).
3. V. M. Goldschmidt, *Naturwissenschaften* **14,** 477 (1926).
4. A. J. Jacobson, B. B. Tofield, and B. E. F. Fender, *Acta Crystallogr. B* **28,** 956–961 (1972).
5. R. L. Cook and A. F. Sammells, *Solid State Ionics* **45,** 311–21 (1991).
6. G. B. Zhang and D. M. Smyth, *Solid State Ionics* **82,** 161–172 (1995).
7. M. T. Anderson, J. T. Vaughey, and K. R. Poeppelmeier, *Chem. Mater.* **5,** 151–165 (1993).
8. C. Greaves, A. J. Jacobson, B. C. Tofield, and B. E. F. Fender, *Acta Crystallogr. B* **31,** 641–646 (1975).
9. K. Mader and H. K. Müller-Buschbaum, *Z. Anorg. Allg. Chem.* **528,** 125–128 (1985).
10. J. B. Goodenough, J. E. Ruiz-Diaz, and Y. S. Zhen, *Solid State Ionics* **44,** 21–31 (1990).
11. S. Adler, S. Russek, J. Reimer, M. Fendorf, A. Stacy, Q. Huang, A. Santoro, J. Lynn, J. Baltisberger, and U. Werner, *Solid State Ionics* **68,** 193–211 (1994).
12. A Manthiram, J. F. Kuo, and J. B. Goodenough, *Solid State Ionics* **62,** 225–234 (1993).
13. S. B. Adler, J. A. Reimer, J. Baltisberger, and U. Werner, *J. Am. Ceram. Soc.* **116,** 675–681 (1994).
14. N. J. G. Gardner, S. Hull, D. A. Keen, and P. Berastegui, Rutherford Appleton Laboratory Report, RAL-TR-1998-032, 1998.
15. S. Hull, R. I. Smith, W. I. F. David, A. C. Hannon, J. Mayers, and R. Cywinski, *Physica B* **180–181,** 1000 (1992).
16. W. I. F. David, R. M. Ibberson, and J. C. Matthewman, Rutherford Appleton Laboratory Report, RAL-92-032, 1992.
17. P. J. Brown and J. C. Matthewman, Rutherford Appleton Laboratory Report, RAL-87-010, 1987.
18. "International Tables for Crystallography" (A. J. C. Wilson, Ed.), Vol. C. Kuwer, Dordrecht, 1995.
19. D. H. Gregory and M. T. Weller, *J. Solid State Chem.* **107,** 134–148 (1993).
20. A. A. Colville, *Acta Crystallogr. B* **26,** 1469–1473 (1970).
21. O. Millat, T. Krekels, G. Van Tendeloo, and S. Amelinckx, *J. Phys. I Fr.* **3,** 1219–1234 (1993).
22. G. Krekels, O. Millat, T. Van Tendeloo, S. Amelinckx, T. G. N. Babu, A. J Wright, and C. Greaves, *J. Solid State Chem.* **105,** 313–335 (1993).
23. A.R. Landa-Cánovas and S. Hansen, *Cement Concrete Res.* **29,** 676–686 (1999).
24. T. B. White, R. L. Segall, J. C. Barry, and J. L. Hutchison, *Acta Crystallogr. B* **41,** 93–98 (1985).
25. J.-C. Grenier, N. Ea, M. Pouchard, and P. Hagenmuller, *J. Solid State Chem.* **58,** 243–252 (1985).
26. R. D. Shannon, *Acta Crystallogr. A* **32** 751 (1976).